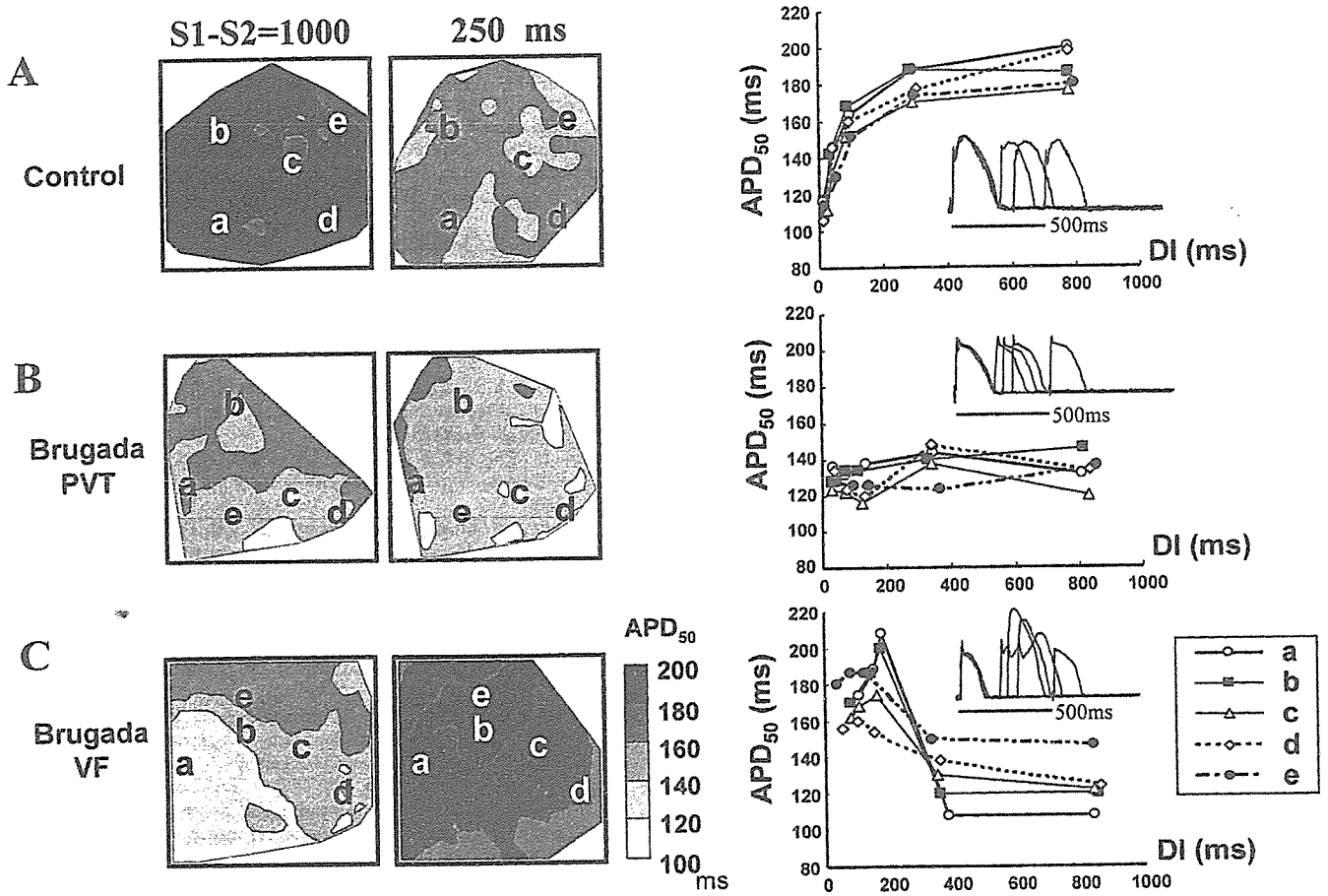


**Figure 9.** Representative epicardial repolarization maps paced from the epicardium by S1-S2 method and plot of the restitution of action potential duration at each site (**a to e**) and superimposed optical action potentials at site b in control condition (**A**), and the Brugada-ECG condition with polymorphic ventricular tachycardia (PVT) (**B**) or ventricular fibrillation (VF) (**C**). $APD_{50}$ = action potential duration at 50% repolarization; DI = diastolic interval.

ization abnormalities were important in the development of VF. Our results, for the first time, revealed how repolarization and depolarization abnormalities interact in developing a trigger of premature ventricular complexes and in maintaining VF in the Brugada-ECG condition. A steep repolarization gradient in the epicardium introduced P2R-extrasystoles and subsequent non-sustained polymorphic VT, and further increased depolarization and repolarization abnormalities maintained VF, thus increasing risk of sudden cardiac death.

**Study limitations.** First, we mapped the epicardial or endocardial surface separately in each condition. Therefore, the two-dimensional mapping technique used in this study provides only limited insights into the number of spiral waves and these re-entrant patterns and could not directly evaluate the relationship between the transmural gradient of repolarization and arrhythmogenesis in the Brugada-ECG condition. A second limitation is the size of wedge preparation. It is unclear whether a polymorphic VT or VF in the wedges can result in those with larger hearts. Third, we pharmacologically created, similarly to the methods of previous studies, the Brugada-phenotype, which could not be a complete surrogate for the Brugada syndrome. Finally, with optical mapping, there is a major concern about motion artifacts that can greatly distort the AP recorded, but our ratio-metric methods can reduce motion artifacts without using an uncoupler.

**Reprint requests and correspondence:** Dr. Wataru Shimizu, Division of Cardiology, Department of Internal Medicine, National Cardiovascular Center, 5-7-1 Fujishiro-dai, Suita, Osaka, 565-8565 Japan. E-mail: wshimizu@hsp.ncvc.go.jp.

## REFERENCES

1. Brugada P, Brugada J. Right bundle branch block, persistent ST-segment elevation and sudden cardiac death: a distinct clinical and electrocardiographic syndrome. A multicenter report. J Am Coll Cardiol 1992;20:1391–6.
2. Wilde AA, Antzelevitch C, Borggrefe M, et al. Proposed diagnostic criteria for the Brugada syndrome: consensus report. Circulation 2002; 106:2514–9.
3. Brugada J, Brugada R, Antzelevitch C, Towbin J, Nademanee K, Brugada P. Long-term follow-up of individuals with the electrocardiographic pattern of right bundle-branch block and ST-segment elevation in precordial leads V1 to V3. Circulation 2002;105:73–8.
4. Antzelevitch C, Brugada P, Borggrefe M, et al. Brugada syndrome: report of the second consensus conference: endorsed by the Heart Rhythm Society and the European Heart Rhythm Association. Circulation 2005;111:659–70.
5. Brugada J, Brugada R, Brugada P. Determinants of sudden cardiac death in individuals with the electrocardiographic pattern of Brugada

syndrome and no previous cardiac arrest. Circulation 2003;108: 3092–6.
6. Priori SG, Napolitano C, Gasparini M, et al. Natural history of Brugada syndrome: insights for risk stratification and management. Circulation 2002;105:1342–7.
7. Antzelevitch C, Brugada P, Brugada J, Brugada R, Towbin JA, Nademanee K. Brugada syndrome: 1992–2002: a historical perspective. J Am Coll Cardiol 2003;41:1665–71.
8. Yan GX, Antzelevitch C. Cellular basis for the Brugada syndrome and other mechanisms of arrhythmogenesis associated with ST-segment elevation. Circulation 1999;100:1660–6.
9. Di Diego JM, Cordeiro JM, Goodrow RJ, et al. Ionic and cellular basis for the predominance of the Brugada syndrome phenotype in males. Circulation 2002;106:2004–11.
10. Fish JM, Antzelevitch C. Role of sodium and calcium channel block in unmasking the Brugada syndrome. Heart Rhythm 2004;1:210–7.
11. Kurita T, Shimizu W, Inagaki M, et al. The electrophysiologic mechanism of ST-segment elevation in Brugada syndrome. J Am Coll Cardiol 2002;40:330–4.
12. Lukas A, Antzelevitch C. Phase 2 re-entry as a mechanism of initiation of circus movement re-entry in canine epicardium exposed to simulated ischemia. Cardiovasc Res 1996;32:593–603.
13. Nademanee K, Veerakul G, Nimmannit S, et al. Arrhythmogenic marker for the sudden unexplained death syndrome in Thai men. Circulation 1997;96:2595–600.
14. Kanda M, Shimizu W, Matsuo K, et al. Electrophysiologic characteristics and implications of induced ventricular fibrillation in symptomatic patients with Brugada syndrome. J Am Coll Cardiol 2002;39: 1799–805.
15. Ikeda T, Sakurada H, Sakabe K, et al. Assessment of noninvasive markers in identifying patients at risk in the Brugada syndrome: insight into risk stratification. J Am Coll Cardiol 2001;37:1628–34.
16. Nagase S, Kusano KF, Morita H, et al. Epicardial electrogram of the right ventricular outflow tract in patients with the Brugada syndrome: using the epicardial lead. J Am Coll Cardiol 2002;39:1992–5.
17. Smits JP, Eckardt L, Probst V, et al. Genotype-phenotype relationship in Brugada syndrome: electrocardiographic features differentiate SCN5A-related patients from non-SCN5A-related patients. J Am Coll Cardiol 2002;40:350–6.
18. Akar FG, Spragg DD, Tunin RS, Kass DA, Tomaselli GF. Mechanisms underlying conduction slowing and arrhythmogenesis in nonischemic dilated cardiomyopathy. Circ Res 2004;95:717–25.
19. Kimura M, Kobayashi T, Owada S, et al. Mechanism of ST elevation and ventricular arrhythmias in an experimental Brugada syndrome model. Circulation 2004;109:125–31.
20. Gray RA, Pertsov AM, Jalife J. Spatial and temporal organization during cardiac fibrillation. Nature 1998;392:75–8.
21. Liu YB, Peter A, Lamp ST, Weiss JN, Chen PS, Lin SF. Spatiotemporal correlation between phase singularities and wavebreaks during ventricular fibrillation. J Cardiovasc Electrophysiol 2003;14:1103–9.
22. Pitzalis MV, Anaclerio M, Iacoviello M, et al. QT-interval prolongation in right precordial leads: an additional electrocardiographic hallmark of Brugada syndrome. J Am Coll Cardiol 2003;42:1632–7.
23. Kakishita M, Kurita T, Matsuo K, et al. Mode of onset of ventricular fibrillation in patients with Brugada syndrome detected by implantable cardioverter defibrillator therapy. J Am Coll Cardiol 2000;36: 1646–53.
24. Morita H, Fukushima-Kusano K, Nagase S, et al. Site-specific arrhythmogenesis in patients with Brugada syndrome. J Cardiovasc Electrophysiol 2003;14:373–9.
25. Krishnan SC, Antzelevitch C. Flecainide-induced arrhythmia in canine ventricular epicardium. Phase 2 re-entry? Circulation 1993;87: 562–72.
26. Miyoshi S, Mitamura H, Fujikura K, et al. A mathematical model of phase 2 re-entry: role of L-type Ca current. Am J Physiol Heart Circ Physiol 2003;284:H1285–94.
27. Chen Q, Kirsch GE, Zhang D, et al. Genetic basis and molecular mechanism for idiopathic ventricular fibrillation. Nature 1998;392: 293–6.
28. Brugada R, Brugada J, Antzelevitch C, et al. Sodium channel blockers identify risk for sudden death in patients with ST-segment elevation and right bundle branch block but structurally normal hearts. Circulation 2000;101:510–5.
29. Shimizu W, Antzelevitch C, Suyama K, et al. Effect of sodium channel blockers on ST segment, QRS duration, and corrected QT interval in patients with Brugada syndrome. J Cardiovasc Electrophysiol 2000; 11:1320–9.
30. Gasparini M, Priori SG, Mantica M, et al. Programmed electrical stimulation in Brugada syndrome: how reproducible are the results? J Cardiovasc Electrophysiol 2002;13:880–7.
31. Wu TJ, Lin SF, Weiss JN, Ting CT, Chen PS. Two types of ventricular fibrillation in isolated rabbit hearts: importance of excitability and action potential duration restitution. Circulation 2002;106: 1859–66.
32. Hisamatsu K, Kusano KF, Morita H, et al. Relationships between depolarization abnormality and repolarization abnormality in patients with Brugada syndrome. J Cardiovasc Electrophysiol 2004;15:870–6.
33. Tukkie R, Sogaard P, Vleugels J, de Groot IK, Wilde AA, Tan HL. Delay in right ventricular activation contributes to Brugada syndrome. Circulation 2004;109:1272–7.

## APPENDIX

For accompanying videos to Figures 5, 6, and 7, please see the online version of this article.

The International Journal of Cardiovascular Imaging (2006) 22: 581–593
DOI 10.1007/s10554-005-9048-5


# Visualization of three-dimensional cardiac electrical excitation using standard heart model and anterior and posterior magnetocardiogram

Kuniomi Ogata[1], Akihiko Kandori[1], Tsuyoshi Miyashita[1], Keiji Tsukada[2], Satoshi Nakatani[3], Wataru Shimizu[3], Hideaki Kanzaki[3], Kunio Miyatake[3], Satsuki Yamada[4], Shigeyuki Watanabe[4] & Iwao Yamaguchi[4]

[1]*Hitachi Ltd., Central Research Laboratory, Kokubunji, Tokyo, Japan;* [2]*Department of Electrical and Electronic Engineering, University of Okayama, Okayama, Japan;* [3]*National Cardiovascular Center, Suita, Osaka, Japan;* [4]*Institute of Clinical Medicine, University of Tsukuba, Tsukuba, Ibaraki, Japan*

Received 2 June 2005; accepted in revised form 19 October 2005

*Key words:* cardiac electrical excitation, current-arrow map, magnetocardiogram, standard heart model

## Abstract

Our aim in this study is to obtain novel three-dimensional (3-D) images of cardiac electrical excitation that include morphological information on the whole heart. We obtain these 3-D images by projecting anterior and posterior two-dimensional (2-D) current-arrow maps (CAMs) onto a 3-D standard heart model. This standard heart model is adjusted to the individual subject's heart position by using the coordinates of the sinus node, which are obtained from magnetocardiogram (MCG) signals. The anterior and posterior CAMs are calculated by taking the orthogonal partial derivatives of the normal component of the anterior and posterior MCGs. After adjusting the base current values of the anterior and posterior CAMs, the adjusted CAMs are projected onto the standard heart model. We generated the projected CAMs (PCAMs) of the six phases (atrial, and ventricular, excitation) for seven healthy subjects. The validity of PCAM was evaluated by extracting the maximal current directions and positions from the PCAMs. The maximal current directions and positions during each excitation phase were almost in the same in the seven healthy subjects. Therefore, the PCAMs give us a clear view of the anterior and posterior myocardial excitation for the respective electrophysiological phases.

## Introduction

Three-dimensional (3-D) electrophysiological information about the heart is a very important tool for analyzing the mechanisms of arrhythmia and ischemic heart disease. In recent years, novel electrophysiological imaging systems have been developed using invasive and noninvasive technologies.

The CARTO [1] and NOGA [2–4] systems were developed to get images of endocardial electrical activity in the atrium and the ventricle by using nonfluoroscopic catheters. These invasive systems use magnetic sensors to precisely detect the catheter position and simultaneously measure the cardiac action potential from electrodes on the catheter. Therefore, these systems display images of endocardial potential mapping with the 3-D anatomy of the heart. These images are used to detect the presence of stunned myocardium [3] and assess myocardial viability in patients with ischemic cardiomyopathy [4]. However, mapping a

large number of points in the endocardium takes too much time [2].

Noninvasive imaging techniques estimate epicardial electrical activity from body surface potential mapping (BSPM) signals. The problem of estimating epicardial electrical activity from BSPM signals is called the bioelectric inverse problem. In the past decade, there has been a significant amount of work on estimation algorithms for solving the bioelectric inverse problem. The present techniques include truncated singular value decomposition [5], Wiener estimation [6], the Gauss-Newton method [7], and computer simulations and animal experimentation [8]. Most of them use the thikhonov regularization method to overcome the non-uniqueness of the inverse problem's solution. However, an optimal regularization parameter has yet to be determined [6].

The magnetocardiogram (MCG) is a novel technology that can produce images of the cardiac electrical excitation in heart muscle. An MCG noninvasively measures the weak magnetic field generated by the adult [9–11] or fetal heart [12] in a way that doesn't require contact with the human body. A two-dimensional (2-D) current-arrow map (CAM) [13] has been proposed as a method for calculating pseudo-cardiac electrical current from MCG signals. Maps of this type are providing the basis for a new method of analyzing atrial excitation of normal subject [14], arrhythmia [15, 16] and ischemic heart disease [17]. Furthermore, multiple activated regions during the ventricular depolarization have been visualized by using the anterior and posterior CAMs [18]. Recently, a method for projecting CAMs onto a 3-D anatomical heart model [19] was developed. The heart model in this case was the entire surface of the heart, and it was created from images obtained by magnetic resonance imaging (MRI). However, this method isn't suitable for practical use, since obtaining an MR image of an individual's heart takes a lot of time.

The aim of our work is to obtain novel 3-D images of cardiac electrical excitation by using a 3-D standard heart model. We started by making the 3-D standard heart model from MR images of three healthy men. This standard heart model was then adjusted to the optimal position for individual subjects by using information on the heart's position. This information takes the form of the coordinates of the sinus node, which is the heart's natural pacemaker; we obtain these coordinates from MCG signals at the early p-wave. The anterior and posterior CAMs are then projected onto the positionally adjusted standard heart model. In our study, we used them to obtain the 3-D image of cardiac electrical excitation for seven healthy subjects.

## Experiment

### *MCG measurement for anterior and posterior plane*

Figure 1a shows the conventional configuration of performing MCG measurements. We used a Low-Tc superconducting quantum interference device (SQUID) system (MC-6400, Hitachi High-Technologies Corporation) with 64 co-axial gradiometers to measure the MCG signals, which are perpendicular components to the anterior chest wall. The magnetic flux resolution of all gradiometers was better than 20 $fTHz^{1/2}$. The SQUID sensors were laid out in an 8 × 8 matrix with a pitch of 25 mm, and the measurement area was 175 × 175 mm. For the anterior chest wall measurement, the patient lie supine on the bed and sensor (7, 3) was placed above the position of the xiphoid process. For the posterior chest wall measurement, a patient is turned around and a sensor (7, 6) was placed directly underneath the position of the xiphoid process. The MCG signals were acquired at a sampling frequency of 1 kHz and passed through band-pass (0.1–100 Hz) and power-line noise filters. The measurement period was 30 s, and the MCG signals for all pulses over this period were averaged. To adjust the time phases of the anterior and posterior MCG signals, we simultaneously measured the Lead II electrocardiogram (ECG) signals.

### *MRI measurement*

Figure 1b shows the configuration for the MRI (Magnex 100 (1T), Shimadzu Corporation) measurement. To visualize the 3-D structure of the entire surface of the heart, MR images were

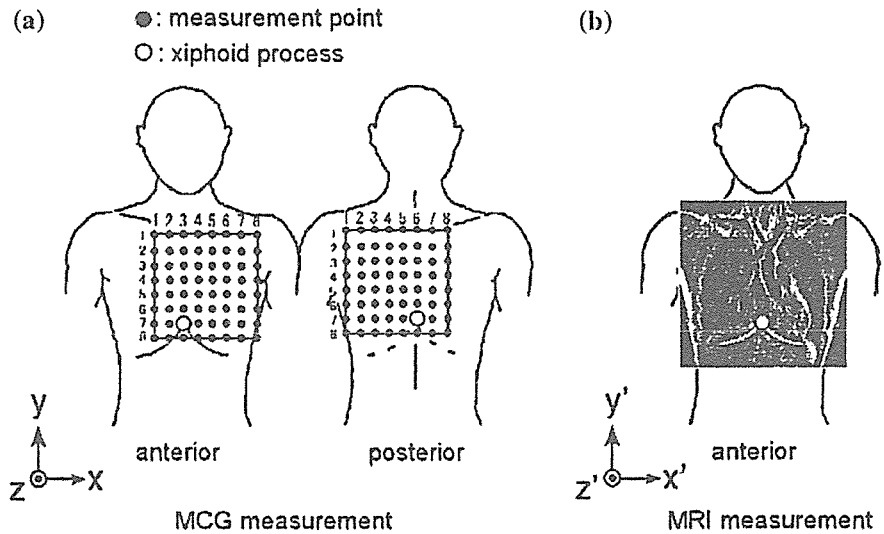


*Figure 1.* Configuration for (a) MCG and (b) MRI measurement. (•: measurement point, O: xiphoid process).

recorded by scanning 300 × 300 mm anterior planes with a lateral separation of 6 mm. ECG triggering controlled the taking of the MR images. Body motions associated with the heartbeat were theoretically corrected by using ECG triggering. The MR examination for one subject was completed within about 30 min.

## Methods

### *Method of making the 3-D standard heart model*

We made the standard heart model, which simulated surface of the whole heart, from MR images of the chests of three healthy adult subjects: subject A (male, 25 years old), subject B (male, 32 years old), subject C (male, 34 years old). After the MR images were obtained, the standard heart model was generated in three steps: (1) Heart-outline points were extracted from each MR image and 3-D heart models for each subject were made from these points. (2) The centroid of the heart models was calculated from all heart-outline points. Then, the distances from the centroid to each point were obtained. (3) The average distances were calculated from these distances for the three subjects and were used to generate the standard heart model.

### *Method of determining the individual heart's position using the 3-D standard heart model*

To be useful, the standard heart model has to be adjusted to an individual's heart position by using the coordinates of the sinus node. The sinus node is located in the right atrium, one of the major elements in the cardiac conduction system that controls heart rate. The sinus impulse excites the right and left atrial myocardium, and these excitations are recorded on the p-wave of the MCG signals. Thus, we assume that the coordinates of the sinus node correspond to the coordinates of a current dipole, which are obtained by applying the equivalent current dipole (ECD) algorithm [20, 21] to the MCG signals at the beginning of the p-wave. The ECD algorithm is a method for estimating the coordinates ($x_d$, $y_d$, $z_d$), angle θ, and moment $Q$ of the current dipole, and these parameters are calculated by minimizing the following equation:

$$F(x_d, y_d, z_d, \theta, Q) = \frac{\sum_{n=1}^{64} \left(B_{t,n} - QL_n(x_d, y_d, z_d, \theta)\right)^2}{\sum_{n=1}^{64} B_{t,n}} \quad (1)$$

where $B_{t,n}$ ($n = 1,2,...,64$) denotes measured MCG signals for the $n$th sensor at instantaneous time $t$.

The coefficient $L_n$ is given by the Biot–Savart law. The method for determining the optimal position for the 3-D standard heart model consists of three steps. (1) Extract the coordinates of the sinus node from the standard heart model. In Figure 2, the coordinates (a) correspond to the sinus node on the 3-D standard heart model. (2) Estimate the position of the current dipole from the MCG signals at the beginning of the p-wave. In Figure 2, coordinates (b) correspond to the estimated current dipole. (3) Superimpose the coordinates of the sinus node (a) on the coordinates of the estimated current dipole (b).

*Method of calculating the CAM*

The CAM reflects the cardiac electrical excitation [13]. The current arrows of the CAM ($\mathbf{I} = (I_x, I_y)$) are calculated by taking orthogonal partial derivatives of the perpendicular components to the anterior chest wall of the magnetic field. In other words, the CAM is calculated from Equations (2) and (3).

$$I_x = \frac{\partial B_z}{\partial y} \tag{2}$$

$$I_y = -\frac{\partial B_z}{\partial x} \tag{3}$$

where $B_z$ indicates the perpendicular components of the measured magnetic field. Spatial derivatives of Equations (2) and (3) are numerically calculated as differences between neighboring points. The magnitude of the current arrow is derived from Equation (4):

$$|I| = \sqrt{(I_x)^2 + (I_y)^2} \tag{4}$$

*Method of projecting the anterior and posterior CAMs onto the 3-D standard heart model*

The CAMs are projected onto the positionally adjusted 3-D standard heart model (section 3.2) by means of a displacement-free mapping of the current vectors onto the corresponding heart-outline points. The anterior and posterior CAMs are projected onto the anterior and posterior surfaces of the standard heart model, respectively. However, the projected CAM (PCAM) has a discontinuous current distribution at the joint of the

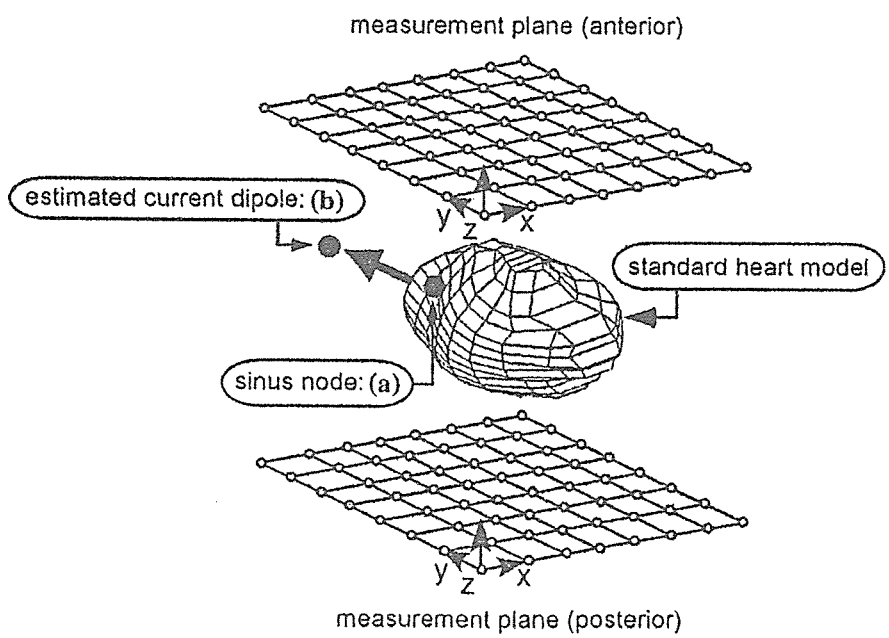


*Figure 2.* Positional adjustment of standard heart model using information on the subject's heart position.

anterior and posterior surface of the standard heart model, since the base currents of the anterior and posterior CAMs are different. This is because the distance between the heart and anterior measurement plane is not equal to the distance between the heart and posterior measurement plane. The method of adjusting the base currents consists of three steps.

(1) Extract the magnitude of the anterior CAM $| I_{f,t}(x_m, y_m) |$ $(m = 1,2,...,M,\ t = 1,2,...,T)$ and posterior CAM $| I_{b,t}(x_m, y_m) |$ on the outermost heart-outline C for the xy plane (see Figure 3). $T$ denotes the total measurement time and $M$ denotes the total number of heart outline point on C.

(2) The weighting coefficient $W$, which adjusts the base currents of the anterior and posterior CAMs, is obtained by minimizing the following equation:

$$F(W) = \sum_{t=1}^{T} \sum_{m=1}^{M} \left( |I_{f,t}(x_m, y_m)| - W \times |I_{b,t}(x_m, y_m)| \right)^2 \tag{5}$$

(3) The anterior CAM and the weighted posterior CAM are projected onto the 3-D standard heart model.

*Method of evaluating the PCAM*

To evaluate the PCAM images, the maximal current direction and position are extracted from the PCAM. The maximal current direction and position reflect the electrical axis of the heart and dominant excitation regions in the heart muscle. Therefore, PCAM could be verified by investigating these values in healthy subjects.

## Simulation

To simulate the magnetic field generated by the human heart, we used a horizontal layered conductor to model the torso and current dipoles to model the cardiac electrical excitation. We compared the PCAMs obtained from simulated magnetic fields for several cases while changing the distances between the current dipoles and measurement planes. In Figure 4, assuming that the

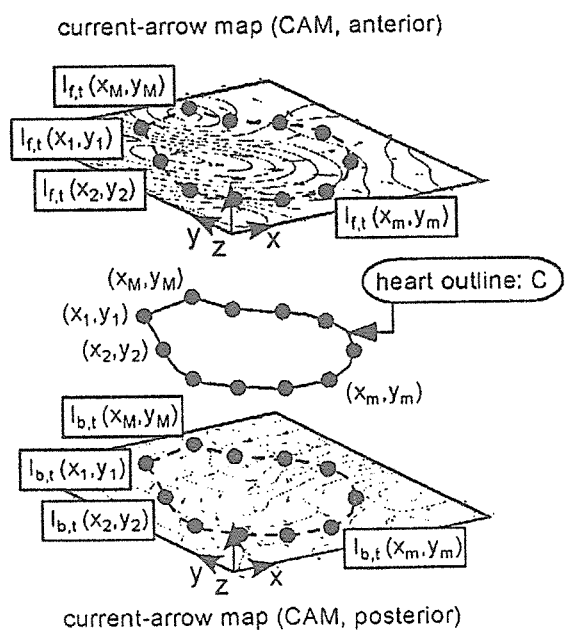


*Figure 3.* Adjustment of base level current in anterior and posterior CAM.

moment of current dipole Q($Q=(Q_x, Q_y, Q_z)$) is located at $r'$ ($r'=r'_x, r'_y, r'_z$) inside the conductor, the anterior magnetic field $B_f(r_f)$ ($B_f(r_f)=[B_{f,x}(r_f)\ B_{f,y}(r_f)\ B_{f,z}(r_f)]^T$) at $r_f$ ($r_f=(r_{f,x}, r_{f,y}, r_{f,z})$) at the measurement points outside the conductor, is expressed using the equation derived by Sarvas [22]

$$B_f(r_f) = \frac{\mu_0}{4\pi K^2}(Q \times a \cdot e_z \nabla K - K e_z \times Q) \quad (6)$$

where $a=r_f-r'$, $a=|a|$, $K=a(a+a\cdot e_z)$, $\nabla K=(2+a^{-1}a\cdot e_z)+ae_z$ and $e_z$ is a unit vector in the perpendicular direction. The posterior magnetic field $B_b(r_b)$ ($B_b(r_b)=[B_{b,x}(r_b)\ B_{b,y}(r_b)\ B_{b,z}(r_b)]^T$) at $r_b$ ($r_b=(r_{b,x}, r_{b,y}, r_{b,z})$) is obtained by changing the subscript f to b of Equation (6). The anterior and posterior measurement planes are assumed to be the xy plane, and the perpendicular direction is assumed to be the $z$-axis. The measurement points are laid out in an 8 × 8 matrix with a pitch of 25 mm. Depth distance $d_f$ denotes the distance between the centroid of the heart model and the anterior measurement plane, and $d_b$ denotes the distance between the centroid and the posterior plane. The anterior and posterior CAMs are calculated from $B_f(r_f)$ and $B_b(r_b)$ using Equations (2) and (3). These CAMs are projected onto the 3-D standard heart model using a weight coefficient $W$.

Figure 5a–d show the simulated results using two dipoles located on the anterior and posterior surfaces of the standard heart model (anterior dipole moment $|Q_f|$ and posterior dipole moment $|Q_b|=50$ nAm, $|Q_f|\ /\ |Q_b|=1$). Figure 5a illustrates the dipoles on the standard heart model. Figure 5b–d illustrate the 3-D images of the PCAMs. To evaluate the simulated PCAM, we used the ratio of the maximal current of the PCAM's front surface to the maximal current of the PCAM's back surface. This value is a measure of $|Q_f|/|Q_b|$. Figure 5b shows the simulated result for $d_f=d_b=100$ mm. The ratio of maximal front and back surface currents is 1.0. Figure 5c shows the simulated result for $d_f=100$ mm and $d_b=125$ mm. The ratio in this case is 1.2. Figure 5d shows the simulated result for $d_f=100$ mm and $d_b=150$ mm. The ratio in this case is 1.3. We see from Figure 5b–d that the

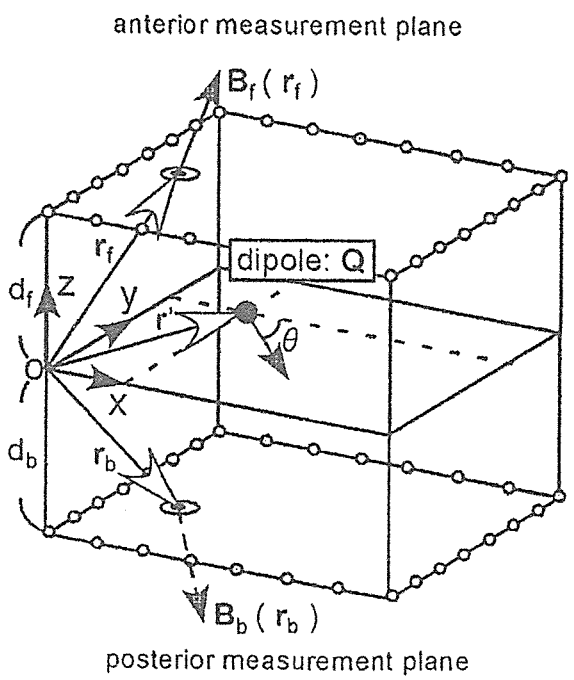


*Figure 4.* Simulation model.

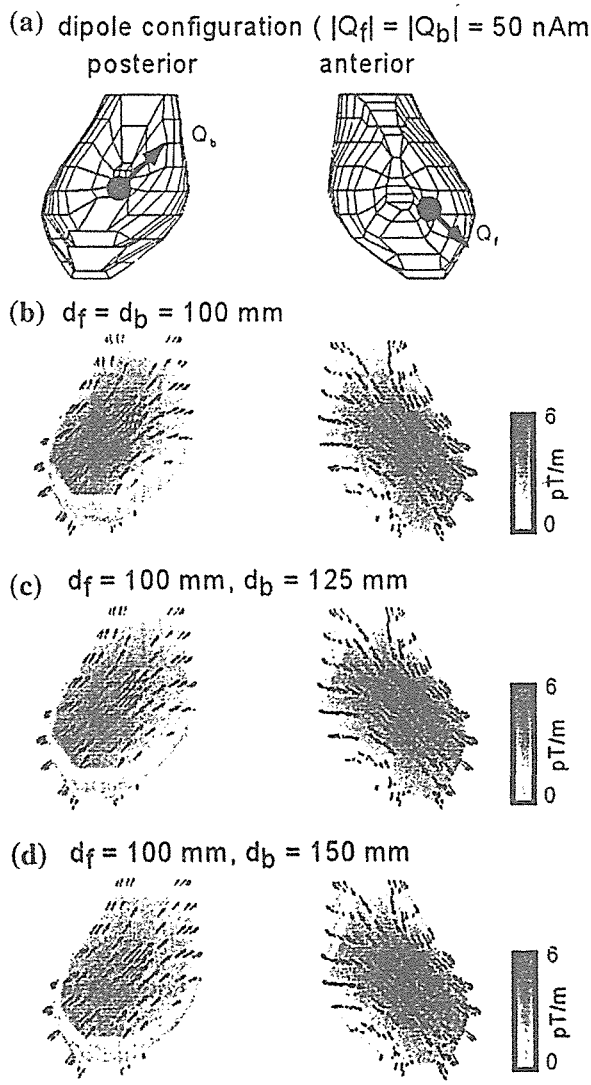


*Figure 5.* Numerical results for several values of distances $d_f$ and $d_b$ [(a) Dipole configuration, (b) $d_f = d_b = 100$ mm case, (c) $d_f = 100$ mm and $d_b = 125$ mm, (d) $d_f = 100$ mm and $d_b = 150$ mm].

maximal current positions and directions on the anterior and posterior surfaces of the heart model corresponded to the assumed dipoles. Furthermore, the ratios of the anterior to posterior maximal currents for each distance are about 1, which indicates that $| Q_f | / | Q_b | = 1$. These simulation results indicate that the PCAMs reflect the anterior and posterior current even if the distances between the heart and anterior and posterior measurement planes are different. Hence, we could apply the PCAM method to actual subject data.

## Experimental results

### *Three-dimensional images of cardiac electrical excitation for a typical healthy subject*

Figure 6a, b show MCG signals of the anterior and posterior measurement planes for one typical healthy subject. The upper figures show grid-maps made from one-beat waveforms of the measured magnetic field. The lower figures show the overlapped waveforms of the all 64 channels for this

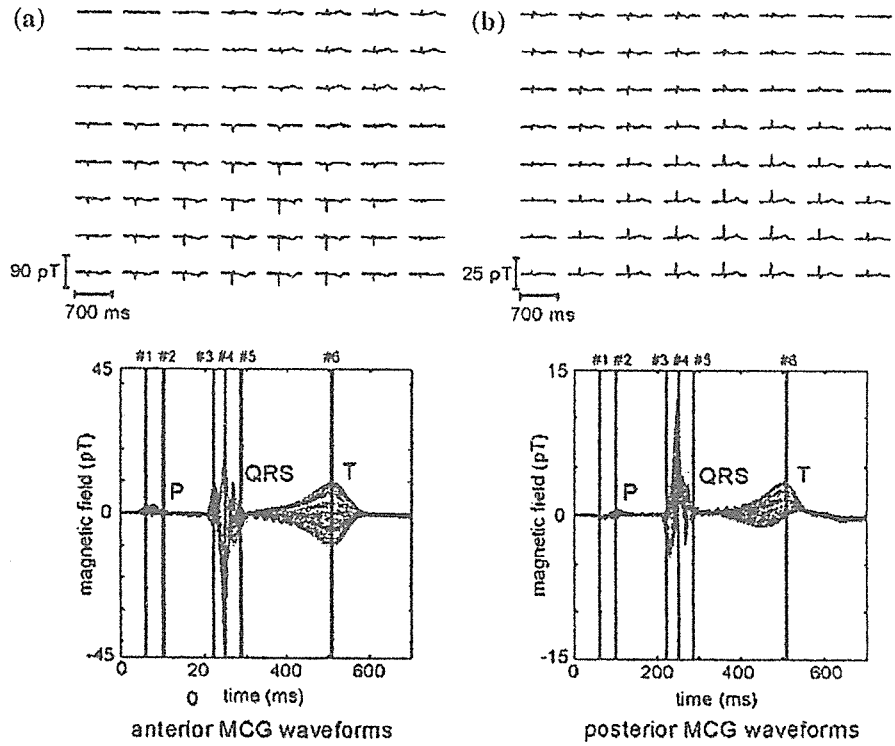


*Figure 6.* Sixty-four-channel MCG waveforms for one typical healthy subject [(a) MCG waveforms for anterior measurement plane, (b) MCG waveforms for posterior measurement plane]. The upper figures are grid-maps and lower ones are overlapped waveforms of all 64 channels. Six lines (#1-#6) in the lower figures correspond to the early p-wave, late p-wave, early QRS-complex, R-wave peak, late QRS-complex and T-wave peak.

subject. Each waveform indicates the temporal change in each magnetic field at 64 measurement points. The lines in the lower figures indicate the six phases (#1: early p-wave (20 ms after p onset), #2: late p-wave (20 ms before end point of p), #3: early QRS-complex (20 ms after Q onset), #4: peak of R-wave, #5: late QRS-complex (20 ms before end point of S), and #6: peak of T-wave at which the six PCAM images in Figure 7a–f were taken. Figure 7 also illustrates the definition of current arrow direction.

Figure 7a, b shows PCAMs during the p-wave. The arrows indicate current direction, and the color-map indicates the magnitude of the current vector. The calculated optimal weighting coefficient $W$ for this subject was 1.86. The high-value area of the PCAM during the early p-wave (#1, see Figure 6) was in the right atrium of the anterior surface of the standard heart model, and the current flow was in the inferior direction in the upper right. During the late p-wave (#2, see Figure 6), the high-value area (red area) was in the left atrium of the posterior surface. Figure 7c–e illustrates PCAMs during the QRS-complex. We see significant map-to-map changes in the direction of the current arrows and position of the high-value areas. The high-value areas during the early QRS-complex (#3, see Figure 6) were in the left ventricle lateral side of the anterior surface and posterior paraseptal. At the R-wave peak (#4, see Figure 6), the maximum-value area was in the left ventricle of the anterior surface. The high-value area during the late QRS-complex (#5, see Figure 6) was in the anterior paraseptal. Figure 7f shows PCAM at the T-wave peak (#6, see Figure 6). Current flow during the T-wave was leftward and in the inferior direction, and high-value area covered the whole ventricle.

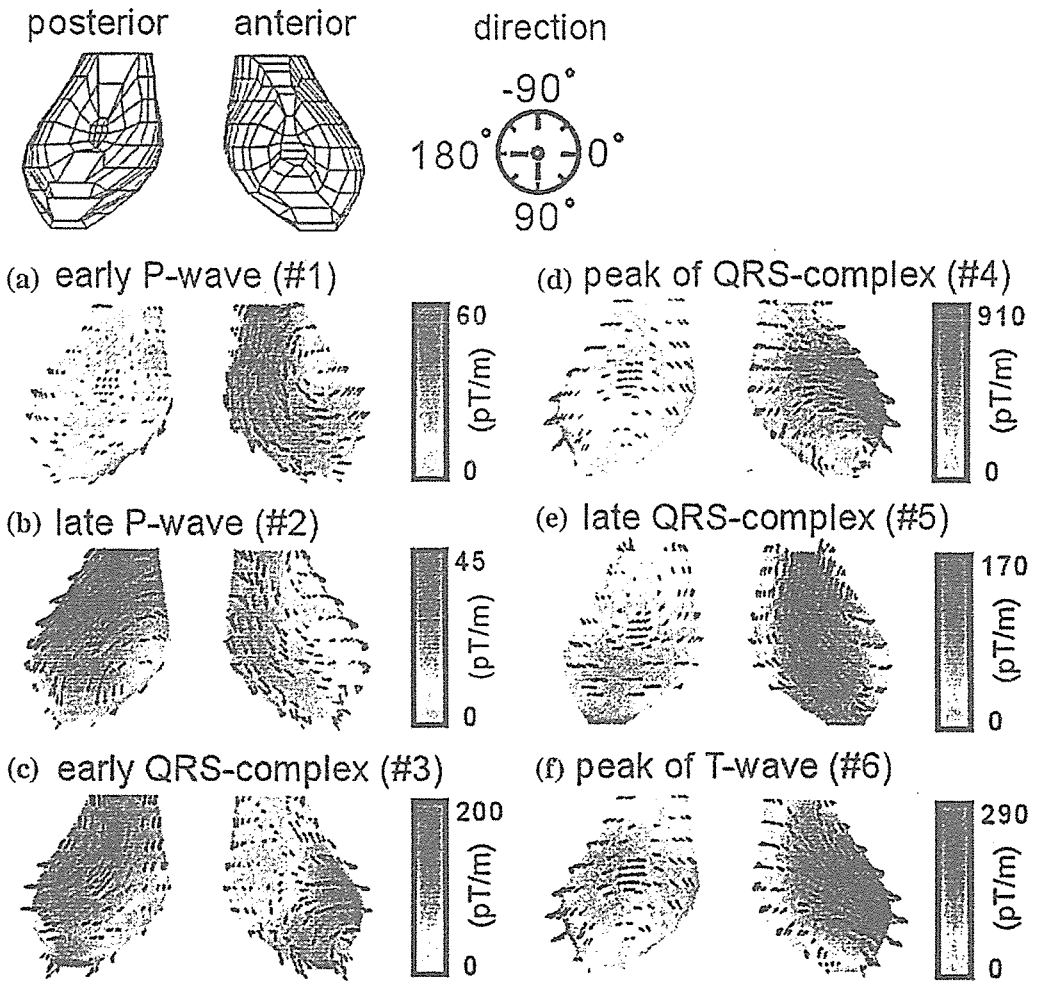


*Figure 7.* PCAMs of six phases for one typical healthy subject [(a) early p-wave, (b) late p-wave, (c) early QRS-complex, (d) peak of R-wave, (e) late QRS-complex, (f) peak of T-wave].

*Maximal current directions and positions on PCAMs for seven healthy subjects*

Figure 8a–e illustrate the direction and position of the maximal current vector during the six electrophysiological phases for seven healthy subjects (male: five, female: two, average age ± SD: 33 ± 6). Table 1 shows the maximal current direction during each phase and average maximal current direction for the seven subjects. During the early p-wave, the maximal current for all subjects appears in the right atrium of the anterior surface, and the average current direction is 72 ± 17 (averaged direction ± SD) degrees. During the late p-wave, the maximal current for all subjects appears in the left atrium of the posterior surface. The average current direction is 17 ± 9 degrees. Figure 8c–e illustrate the maximal current position and direction for the early QRS-complex, R-wave peak, and late QRS-complex, respectively. During the early QRS-complex, the maximal current of six of the seven subjects appears in the left ventricle, whereas the maximal current of one of the seven appears in the ventricular septum. The average current direction is 142 ± 44 degrees. During the R-wave peak, the maximal current for all subjects appears in left ventricle of the anterior and posterior surfaces, and average current direction is 35 ± 13 degrees. During the late QRS-complex, the maximal current of six of the seven subjects

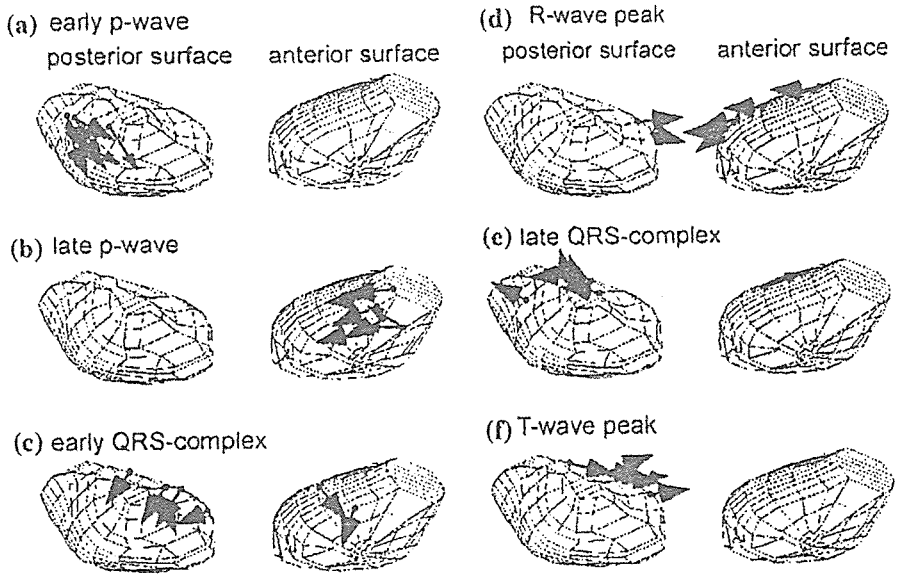


*Figure 8.* Maximal current vector of PCAMs of six phases for seven healthy subjects [(a) early p-wave, (b) late p-wave, (c) early QRS-complex, (d) R-wave peak, (e) late QRS-complex, (f) T-wave peak].

*Table 1.* Maximum current directions during each electrophysiological phase for seven healthy subjects.

| ID No. | Age/Sex | $P_b$ (degree) | $P_e$ (degree) | $QRS_b$ (degree) | $R_{max}$ (degree) | $QRS_e$ (degree) | $T_{max}$ (degree) |
|---|---|---|---|---|---|---|---|
| N 1 | 43/M | 23 | 8 | 162 | 26 | −133 | 38 |
| N 2 | 24/M | 90 | 20 | 10 | 32 | −63 | 45 |
| N 3 | 29/M | 65 | 13 | 102 | 32 | −141 | 11 |
| N 4 | 43/M | 76 | 9 | 159 | 46 | −147 | 40 |
| N 5 | 35/F | 96 | 26 | −156 | 68 | −137 | 41 |
| N 6 | 25/M | 83 | 36 | −175 | 32 | −157 | 31 |
| N 7 | 29/F | 60 | 9 | 174 | 42 | −117 | 30 |
| Mean ± SD | 33 ± 6 | 72 ± 17 | 17 ± 9 | 142 ± 44 | 35 ± 13 | −136 ± 23 | 31 ± 8 |

appears in the upper ventricular septum of the model's anterior surface and the average current direction is −136 ± 23 degrees. Figure 8f illustrates the maximal current and direction for the T-wave peak. At the T-wave peak, the maximal current for all subjects appears in the left ventricle of the anterior and posterior surfaces and the average current direction is 33 ± 8 degrees.

## Discussion

### *Electrophysiological phenomena in the healthy heart*

To visualize the cardiac electrical excitation, we projected CAMs, which are calculated from MCG signals that corresponded to the p-wave, QRS-complex and T-wave, onto a 3-D standard heart model. The electrical activity in the p-wave should reflect right-atrial excitation, right and left atrial excitation, and left atrial excitation [23]. The PCAMs during the p-wave are seen in Figure 7a, b. During the early p-wave, the high-value area is in the right atrium of the model's anterior surface. In the later stage, the region of greatest activity shifts toward the left atrium of the model's posterior surface. The similar results during the p-wave for healthy subjects are reported using the anterior and posterior 2-D CAMs [24].

The QRS-complex reflects ventricular depolarization. Figure 7c–e show the PCAMs during the QRS-complex. During the early QRS-complex, the

high-value areas are in the ventricular septum and left ventricle. The current direction in the ventricular septum of the anterior surface is differs from the current direction in the left ventricle of the posterior surface. These multi-activated regions were observed in all subjects. The existence of multi-activated regions during the early QRS-complex has been reported based on electrophysiological measurements made on several isolated hearts [23]. We found that PCAMs detect the multiple electrical activities in heart muscle. At the peak of the R-wave, the highest value is in the left ventricle; its strength reflects the high myocardium volume of the left ventricle. During the last stage, high-value area shifts toward the upper region of the ventricle. The last parts to be activated are the posterobasal area, pulmonary conus [23] and the upper ventricular septum [25]. In this subject, therefore, we found that the high-value area in the last stage mainly reflects the electrical activity of the upper ventricular septum.

The T-wave reflects ventricular repolarization. Figure 7f shows the PCAM at the T-wave peak. The high-value area of the PCAM covers the whole ventricle, and current flow is leftward and in the inferior direction. The current direction is the same as at the QRS-complex peak. As a result, we can say that the respective PCAMs of Figure 7a–f strongly reflect the respective electrophysiological phases (p-wave, QRS-complex and T-wave).

*Evaluating the validity of PCAM using maximal current direction and position*

To evaluate the validity of the PCAM method, we extracted the maximal current direction and position from the PCAM for seven healthy subjects. In Figure 8a, b, the maximal current positions for seven healthy subjects during the early and late p-wave appear at almost the same positions on the anterior and posterior surfaces of the PCAMs. The average direction of early and late p-waves are $72 \pm 17$ and $17 \pm 9$ degree, respectively (see Table 1). The SDs of the average current direction during the p-wave are within 20 degrees. These values are small in comparison with the total angle (360 degrees). The electrical activities in the early and late p-waves reflect the excitation of the right and left atrial myocardium [14, 23]. Since the right and left atrial myocardia are relatively thin walled and small, the atrial myocardial excitation is comparatively localized. Therefore, we see that the maximum current directions and positions during the p-wave for the seven healthy subjects are in the same anatomical sites and directions. In Figure 8c–f, unlike the maximal current positions during the p-wave phases, the maximal current positions during the ventricular excitations differ. The average directions during the early QRS-complex, R-wave peak, late QRS-complex and T-wave peak are $142 \pm 44$ ms, $35 \pm 13$, $-136 \pm 23$ and $31 \pm 8$ degrees (see Table 1). The excitation regions of the QRS complex rapidly spread over the whole ventricle [23] and there are several activated regions in the ventricle.

As a result, the maximal current directions and position during the p-wave and the maximal current directions during the QRS-complex nearly coincided for the seven healthy subjects, which shows the validity of PCAM.

*Comparison with other methods of calculating cardiac-electrical current*

There are two other ways to get a visual depiction of cardiac electrical excitation from MCG signals. One way is to estimate the 3-D localization and strength of a single-current dipole for arrayed MCG signals [20, 21]. A single dipole can optimally localize the pre-excitation activity and this localization has a numerical error of about 10 mm [21]. In clinical application, this method can localize the early ventricular depolarization sites of WPW syndrome [20] and estimate the electrical activity of the fetal heart [12]. However, it is difficult for this estimation to be used to calculate a cardiac electrical current with a wide distribution in the ventricular excitation.

The second way is to solve a nonlinear biomagnetic inverse problem for arrayed MCG signals. Inversion techniques that can be used to estimate the cardiac electrical current of wide distributions include the Wiener filter [26] and minimum-norm method (MNM) [27]. Furthermore, computer simulation of MNM can locate ischemic areas using simulated MCG signals [27]. Regularization

techniques are used to overcome the ill-posed qualities (the discontinuities, non-uniqueness) of the nonlinear biomagnetic inverse problem. However, estimating the correct unique solution for cardiac electrical current of a wide distribution remains difficult because a technique for finding the optimal regularization parameter has not yet been developed.

On the other hand, we use 2-D CAMs [13] to get the image of the cardiac electrical excitation. The CAMs has been proposed as a method for calculating pseudo cardiac electrical current from MCG. However, CAMs provide the basis for a new method for the diagnosis of atrial flutter [15], long QT syndrome [16], coronary artery disease [17], and fetal WPW syndrome [28]. Therefore, we think that a CAM is very useful for visualizing the images of cardiac electrical excitation.

*Limitations of the PCAM method*

There are several limitations to the PCAM method. First, it is difficult for PCAM to visualize the cardiac electrical current of the patient with abnormal heart rhythm, such as atrial fibrillation (Af), atrial flutter (AF) and ventricular fibrillation (Vf). To generate the PCAM images for these patients, we have to use non-averaging anterior and posterior MCG signals corresponding to the same cardiac excitation phase. However, the MCG system can not measured the anterior and posterior MCGs simultaneously. Moreover, the PCAM method can not apply to high-risk patient with congestive heart failure, who can not lay on the front on the bed. A MCG system, which measures the anterior and posterior MCG simultaneously, may be needed if we overcame these problems.

Secondly, a standard heart model does not express an individual subject's heart exactly and cardiac contraction. Therefore, it is difficult for PCAM to visualize the exactly image of cardiac current to the patient with abnormality of heart size and shape, such as hypertrophy. We need individual's 3-D heart model, which is generated by MR images, to solve this problem.

Thirdly, the method for determining the optimal position of standard heart model using the coordinate of the sinus node has a numerical error of about 10–20 mm [29]. Therefore, this method can not adjust the optimal position of the standard heart model for patients with irregular sinus node, such as AF and Af. To overcome this problem, it is deemed desirable to determine the position of the standard heart model by using position of xiphoid process, which is given by position of the sensor (7, 3) for anterior measurement plane.

Despite these limitations, the PCAM method gives us a clear view of the activated region and direction of current flow in the heart muscle.

## References


1. Gepstein L, Hayam G, Ben-Haim SA. A novel method for nonfluoroscopic catheter-based Electroanatomical mapping of the heart. Circulation 1997; 95(6): 1611–1622.
2. Lessick J, Hayam G, Zaretsky A, Reisner SA, Schwartz Y, Ben-Haim SA. Evaluation of inotropic changes in ventricular function by NOGA mapping: comparison with echocardiography. J Appl Physiol 2002; 93: 418–426.
3. Kobayashi Y, Shimada K, Yamagishi H, et al. Left ventricular electromechanical mapping in stunned myocardium. Circulation 2000; 102: e25–e26.
4. Bøtker HE, Lassen JF, Hermansen F, et al. Electromechanical mapping for detection of myocardial viability in patients with ischemic cardiomyopathy. Circulation 2001; 103: 1631–1637.
5. Greensite F, Huiskamp G. An improved method for estimating epicardial potentials from the body surface. IEEE Trans Biomed Eng 1998; 45(1): 98–104.
6. van Oosterom A. The use of the spatial covariance in computing pericardial potentials. IEEE Trans Biomed Eng 1999; 46(7): 778–787.
7. Modre R, Tilg B, Fischer G, Wach P. Noninvasive myocardial activation time imaging: a novel inverse algorithm applied to clinical ECG mapping data. IEEE Trans Biomed Eng 2002; 49(10): 1153–1161.
8. Burnes JE, Taccardi B, Rudy Y. A noninvasive imaging modality for cardiac arrhythmias. Circulation 2000; 102: 2152–2158.
9. Hosaka H, Cohen D. Visual determination of generators of the magnetocardiogram. J Electrocardiol 1976; 9(4): 426–432.
10. Nakaya Y, Sumi M, Saito K, Fujino K, Murakami M, Mori H. Analysis of current source of the heart using isomagnetic and vector arrow maps. Jpn Heart J 1984; 25(5): 701–711.
11. Tsukada K, Haruta Y, Adachi A, et al. Multichannel SQUID system detecting tangential components of the cardiac magnetic field. Rev Sci Instrum 1995; 66(10): 5085–5091.
12. Horigome H, Siono J, Shigemitsu S, et al. Detection of cardiac hypertrophy in the fetus by approximation of the

current dipole using magnetocardiography. Pediatr Res 2001; 50(2): 242–245.
13. Miyashita T, Kandori A, Tsukada K, et al. Construction of tangential vectors from normal cardiac magnetic field components. Proceedings of the 20th annual international conference of the IEEE engineering in medicine and biology society. 1998 October 29–November 1: 520–523.
14. Kuusisto J, Koskinen R, Mäntynen V, et al. Diversity in activation of healthy atria by magnetocardiographic gradient analysis. In: Proceedings of the 14th International Conference on Biomagnetism. 2004 August 8–12, 407–408.
15. Yamada S, Tsukada K, Miyashita T, Kuga K, Yamaguchi I. Noninvasive, direct visualization of macro-reentrant circuits by using magnetocardiograms: initiation and persistence of atrial flutter. Europace 2003; 5: 343–350.
16. Kandori A, Shimizu W, Yokokawa M, et al. Detection of spatial repolarization abnormalities is patients with LQT1 and LQT2 forms of congenital long-QT syndrome. Physiol Meas 2002; 23: 603–614.
17. Kanzaki H, Nakatani S, Kandori A, Tsukada K, Miyatake K. A new screening method to diagnose coronary artery disease using multichannel magnetocardiogram and simple exercise. Basic Res Cardiol 2003; 98: 124–132.
18. Tsukada K, Mitsui T, Terada Y, Horigome H, Yamaguchi I. Noninvasive visualization of multiple simultaneously activated regions on torso magnetocardiographic maps during ventricular depolarization. J Electrocardiol 1999; 32(4): 305–313.
19. Ogata K, Kandori A, Miyashita T, Tsukada K. Visualization method of current distribution in cardiac muscle using a heart model. Trans Jpn Soc Med Biol Eng 2003; 41(1): 25–33.
20. Nomura M, Nakaya Y, Saito K, et al. Noninvasive localization of accessory pathways by magnetocardiographic imaging. Clin Cardiol 1994; 17: 239–44.
21. Hren R, Stroink G, Horáček BM. Accuracy of single-dipole inverse solution when localizing ventricular pre-excitation sites: simulation study. Med Biol Eng Comput 1998; 36: 323–329.
22. Sarvas J. Basic mathematical and electromagnetic concepts of the biomagnetic inverse problem. Phys Med Biol 1987; 32(1): 11–22.
23. Durrer D, van Dam RTh, Freud GE, Janse MJ, Meijler FL, Arzbaecher RC. Total excitation of the isolated human heart. Circulation 1970; 41: 899–912.
24. Sato M, Terada Y, Mitsui T, Miyashita T, Kandori A, Tsukada K. Visualization of atrial excitation by magnetocardiogram. Int J Cardiac Imaging 2002; 18: 305–312.
25. Goldman MJ Principles of Clinical Electrocardiography. California: Lange Medical Publications, 1986.
26. Smith WE. Estimation of the spatio-temporal correlations of biological electrical sources from their magnetic field. IEEE Trans Biomed Eng 1992; 39: 997–1004.
27. Killmann R, Jaros GG, Wach P, et al. Localisation of myocardial ischemia from the magnetocardiogram using current density reconstruction method: computer simulation study. Med Biol Eng Comput 1995; 33: 643–651.
28. Kandori A, Hosono T, Chiba Y, et al. Classifying cases of fetal Wolff–Parkinson-White syndrome by estimating the accessory pathway from fetal magnetocardiograms. Med Biol Eng Comput 2003; 41: 33–39.
29. Ogata K, Kandori A, Miyashita T, et al. Projecting cardiac-current images onto a 3-D standard heart model. In: Proceedings of the 25th Annual International Conference of the IEEE Engineering in Medicine and Biology Society. 2003 17–21 September, pp. 517–520.

*Address for correspondence*: Kuniomi Ogata, Hitachi Ltd., Central Research Laboratory, 1-280 HigashiKoigakubo, Kokubunji, Tokyo, 185-8601, Japan
E-mail: k-ogata@rd.hitachi.co.jp

# Pilsicainide-Induced Verapamil Sensitive Idiopathic Left Ventricular Tachycardia

TAKAYUKI NAGAI, KAZUHIRO SUYAMA, WATARU SHIMIZU, TAKASHI NODA, KAZUHIRO SATOMI, TAKASHI KURITA, NAOHIKO AIHARA, and SHIRO KAMAKURA

From the Division of Cardiology, Department of Internal Medicine, National Cardiovascular Center, Suita, Osaka, Japan

*A 20-year-old man was admitted to our hospital for treatment of verapamil sensitive idiopathic left ventricular tachycardia (ILVT). During the electrophysiologic study (EPS), no sustained ventricular tachycardia (VT) could be induced both at baseline and after infusion of isoproterenol. However, sustained clinical VT could be easily induced with single ventricular extrastimulation following intravenous administration of pilsicainide, a class Ic sodium channel blocker. The arrhythmia was ablated with radiofrequency catheter ablation. (PACE 2006; 29:549–552)*

***verapamil sensitive ventricular tachycardia, radiofrequency catheter ablation, pilsicainide, noninducible sustained ventricular tachycardia***

## Introduction

The clinical usefulness of catheter ablation (CA) for idiopathic left ventricular tachycardia (ILVT) has been well-established,[1,2] and it is regarded as a first-line therapy especially for drug-refractory patients. However, the complete success of ablation procedure depends on the induction of sustained tachycardia. We present here a case with ILVT, in whom sustained tachycardia could be induced by ventricular extrastimulation only in the presence of intravenous pilsicainide.

Address for reprints: Kazuhiro Suyama, M.D., Ph.D., Division of Cardiology, Department of Internal Medicine, National Cardiovascular Center, 5-7-1 Fujishiro-dai, Suita, Osaka 565-8565 Japan. Fax: (81)6-6872-7486; e-mail: ksuyama@hsp.ncvc.go.jp

Received November 11, 2005; revised December 6, 2005; accepted December 19, 2005.

## Case Report

A 20-year-old man presented recurrent episodes of palpitation precipitated by exertion since 2002. His 12-lead electrocardiogram during sinus rhythm showed the saddle-back like ST segment elevation in lead V2 (Fig. 1A). His 12-lead

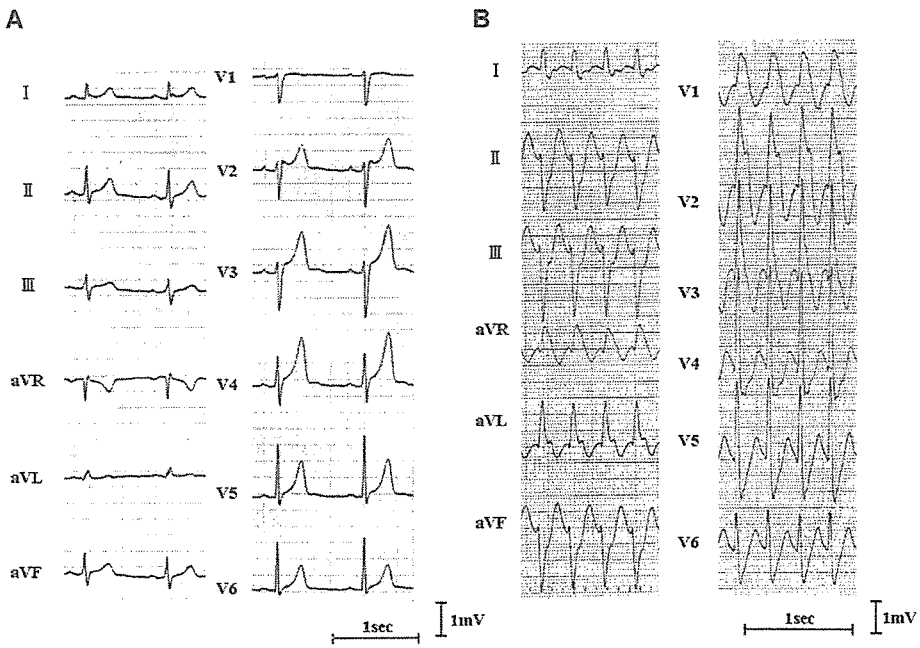


**Figure 1.** *(A) A 12-lead electrocardiogram during sinus rhythm. (B) A 12-lead electrocardiogram of wide QRS complex tachycardia showing right bundle branch block and superior axis morphology.*

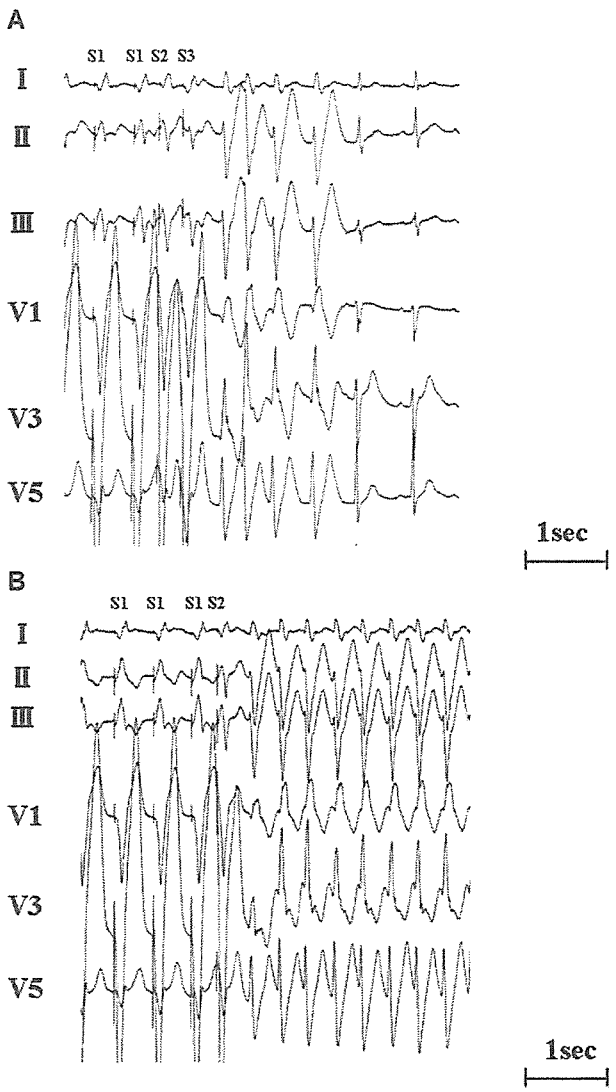


**Figure 2.** *(A) A 6-lead electrocardiogram showing 4-beat runs of PVCs induced by right ventricular double extrastimulation after administration of isoproterenol. (B) A 6-lead electrocardiogram during ventricular tachycardia sustained by right ventricular single extrastimulation after pilsicainide infusion.*

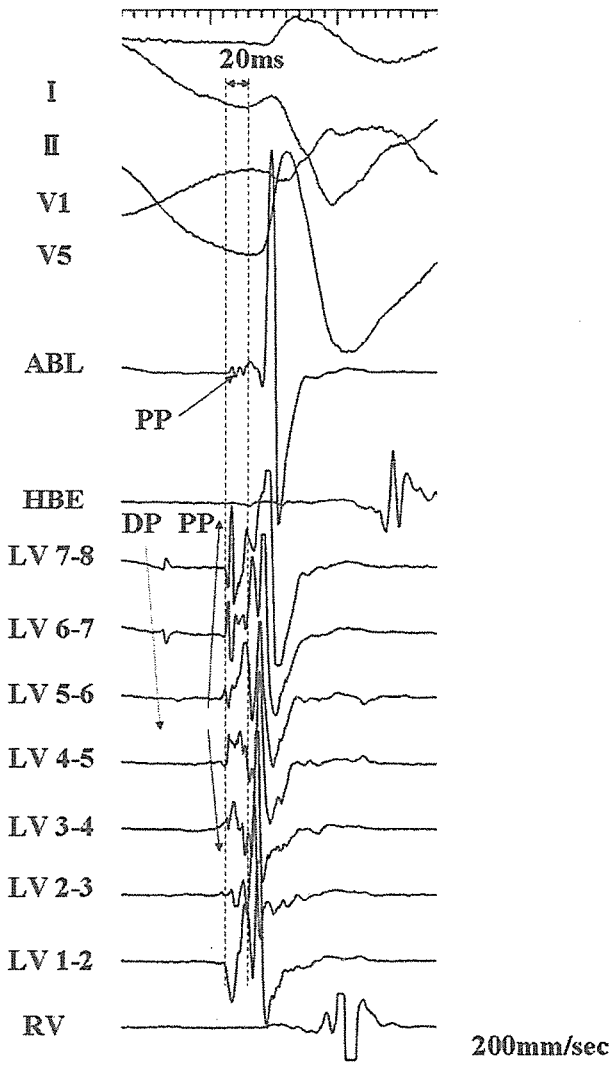


**Figure 3.** *Intracardiac recordings of the successful ablation site during ventricular tachycardia. Both Purkinje potentials (PPs) and diastolic potentials (DPs) are identified by octapolar mapping catheter (LV) positioned at inferoposterior left ventricular septum and the earliest PP is localized in LV 5–6. Radiofrequency application was delivered at the earliest PP which preceded QRS by 20 ms. ABL = ablation; HBE = His bundle electrogram; RV = right ventricle.*

electrocardiogram during palpitation revealed a wide QRS complex tachycardia with right bundle branch block and superior axis morphology (Fig. 1B), suggesting the ventricular tachycardia (VT) originating from left posterior Purkinje network. During the tachycardia, the heart rate was 180 beats/min and the blood pressure was 110/70 mmHg. Intravenous administration of verapamil slowed down and subsequently terminated the tachycardia.[3–5] No structural abnormalities were detected by echocardiography. Therefore, the sustained tachycardia was diagnosed as ILVT. He was referred to our electrophysiologic laboratory to undergo CA in December 2004.

After providing written informed consent, he underwent electrophysiologic study (EPS) in the fasting state. Three standard quadripolar electorode catheters were positioned at high lateral right atrium, His bundle, and right ventricle from both the femoral veins. Under baseline condition, neither nonsustained nor sustained VT could be induced by up to triple extrastimulation and

burst pacing from the right atrium and the right ventricle. During isoproterenol infusion (1.5–2.0 μg/min), only 4-beat runs of premature ventricular complexes (PVCs) were induced (Fig. 2A). The electrocardiographic morphology of the PVCs was identical to the clinical sustained VT.

Left ventricular endocardial mapping was performed with an octapolar electorode catheter introduced from the left femoral artery. Although Purkinje potential (PP) which preceded ventricular electrogram at the inferoposterior left ventricular septum was recorded, during the PVCs, diastolic potential (DP) could not be identified. After intravenous injection of pilsicainide (0.14 mg/kg over a minute period), the sustained tachycardia could be induced by right ventricular single extrastimulation (Fig. 2B), and DP as well as PP could be recorded by octapolar mapping catheter during the tachycardia. A 7-F quadripolar electorode ablation catheter was positioned via the right femoral artery, but it could not record DP during subsequent endocardial mapping. Thus, radiofrequency current was applied to the earliest activation site of PP during VT (Fig. 3), and the sustained tachycardia was terminated after 1.5 seconds of the first application. At the end of the procedure, both VT and PVCs were rendered noninducible despite additional injection of pilsicainide (0.14 mg/kg over a minute period). Although baseline electrocardiogram at sinus rhythm showed the saddle-back like ST segment elevation in lead V2, which suggested potent Brugada syndrome, no additional elevation of ST segment in right precordial leads could be seen after intravenous injection of pilsicainide during EPS. At 10-month follow-up, the patient has remained free of arrhythmia recurrence.

## Discussion

ILVT is characterized as a tachycardia with right bundle branch block and superior axis morphology originating from Purkinje network of the left ventricular septum. The mechanism of ILVT has been supposed to be reentry.[6–13] Although both pace mapping method and endocardial mapping method are used for CA, successful CA has been reported to be achieved mainly ablating DP or earliest PP site at the inferoposterior left ventricular septum during sustained VT by using endocardial mapping method.[1,2,10–13] The induction of sustained VT is, therefore, essential for accurate endocardial mapping and successful CA. Friedman et al. reported a case of noninducible ILVT for which CA was performed by targeting PVCs of the same morphology to the clinical tachycardia using a noncontact mapping system.[14] However, the appropriate site of ablation is still difficult to be identified in cases without induction of sustained VT.

Because the slow conduction zone of reentrant circuit of ILVT appears to depend on the slow inward calcium current, verapamil can terminate the tachycardia. When the magnitude of the slow inward calcium current is not enough to induce and sustain the tachycardia under baseline condition, isoproterenol infusion, which amplifies the current through stimulation of cAMP, is used after for facilitation of inducing the sustained VT.[15] In the present case, we demonstrate the effectiveness of pilsicainide, which is classified as class Ic antiarrhythmic drug and has a pure sodium channel blocking effect, as a facilitator of sustained ILVT. To our knowledge, this is the first reported case of ILVT, which could be induced only in the presence of a sodium channel blocking agent.

The precise mechanism of the induction of sustained VT only after pilsicainide administration is unclear. Tsuchiya et al. showed that a small dose of lidocaine prolonged the cycle length of ILVT, and suggested that not only calcium channel blocking effect, but also sodium channel blocking effect can affect conduction within the myocardium of reentrant circuit of ILVT.[16] Because the mechanism of ILVT is reentry with an excitable gap, increased conduction delay within the reentrant circuit by pilsicainide is likely to be relevant for provocating and/or sustaining the tachycardia, although it is unknown how and where pilsicainide affected conduction within the reentrant circuit.

In this present case report, we demonstrate the potential proarrhythmic effect of pilsicainide (and other drugs which have similar pharmacological action) in ILVT. This medication may be beneficial in patients with ILVT who have no inducible VT at EPS during CA.

## References


1. Nakagawa H, Beckman KJ, McClelland JH, et al. Radiofrequency catheter ablation of idiopathic left ventricular tachycardia guided by a Purkinje potential. Circulation 1993; 88:2607–2617.
2. Wen MS, Yeh SJ, Wang CC, Lin FC, Wu D. Radiofrequency ablation therapy in idiopathic left ventricular tachycardia with no obvious structural heart disease. Circulation 1994; 89:1690–1696.
3. Belhassen B, Rotmensch H, Laniado S. Response of recurrent sustained ventricular tachycardia to verapamil. Br Heart J 1981; 46:679–682.
4. Belhassen B, Shapira I, Pelleg A, Copperman I, Kauli N, Laniado S. Idiopathic recurrent sustained ventricular tachycardia responsive to verapamil: An ECG-electrophysiologic entity. Am Heart J 1984; 108:1034–1036.
5. Lin FC, Finley CD, Rahimtoola SH, Wu D. Idiopathic paroxysmal ventricular tachycardia with a QRS pattern of right bundle branch block and left axis deviation: A unique clinical entity with specific properties. Am J Cardiol 1983; 52:95–100.
6. Ohe T, Shimomura K, Aihara N, et al. Idiopathic sustained left ventricular tachycardia: Clinical and electrophysiologic characteristics. Circulation 1988; 77:560–568.

7. Okumura K, Matsuyama K, Miyagi H, Tsuchiya T, Yasue H. Entrainment of idiopathic ventricular tachycardia of left ventricular origin with evidence for reentry with an area of slow conduction and effect of verapamil. Am J Cardiol 1988; 62:727–732.
8. Maruyama M, Tadera T, Miyamoto S, Ino T. Demonstration of the reentrant circuit of verapamil-sensitive idiopathic left ventricular tachycardia: Direct evidence for macroreentry as the underlying mechanism. J Cardiovasc Electrophysiol 2001; 12:968–972.
9. Ouyang F, Cappato R, Ernst S, et al. Electroanatomic substrate of idiopathic left ventricular tachycardia: Unidirectional block and macroreentry within the Purkinje network. Circulation 2002; 105:462–469.
10. Aiba T, Suyama K, Aihara N, et al. The role of Purkinje and pre-Purkinje potentials in the reentrant circuit of verapamil-sensitive idiopathic LV tachycardia. Pacing Clin Electrophysiol 2001; 24:333–344.
11. Nogami A, Naito S, Tada H, et al. Demonstration of diastolic and presystolic Purkinje potentials as critical potentials in a macroreentry circuit of verapamil-sensitive idiopathic left ventricular tachycardia. J Am Coll Cardiol 2000; 36:811–823.
12. Aiba T, Suyama K, Matsuo K, et al. Mid-diastolic potential is related to the reentrant circuit in a patient with verapamil-sensitive idiopathic left ventricular tachycardia. J Cardiovasc Electrophysiol 1998; 9:1004–1007.
13. Tsuchiya T, Okumura K, Honda T, et al. Significance of late diastolic potential preceding Purkinje potential in verapamil-sensitive idiopathic left ventricular tachycardias. Circulation 1999; 99:2408–2413.
14. Friedman PA, Beinborn DA, Schultz J, Hammill SC. Ablation of noninducible idiopathic left ventricular tachycardia using a noncontact map acquired from a premature complex with tachycardia morphology. Pacing Clin Electrophysiol 2000; 23:1311–1314.
15. Lee KL, Lauer MR, Young C, et al. Spectrum of electrophysiologic and electropharmacologic characteristics of verapamil-sensitive ventricular tachycardia in patients without structural heart disease. Am J Cardiol 1996; 77:967–973.
16. Tsuchiya T, Okumura K, Honda T, Iwasa A, Ashikaga K. Effects of verapamil and lidocaine on two components of the re-entry circuit of verapamil-sensitive idiopathic left ventricular tachycardia. J Am Coll Cardiol 2001; 37:1415–1421.

# Unique electrophysiologic characteristics of atrioventricular nodal reentrant tachycardia with different ventriculoatrial block patterns: Effects of slow pathway ablation and insights into the location of the reentrant circuit

**Kiyoshi Otomo, MD, Hideo Okamura, MD, Takashi Noda, MD, Kazuhiro Satomi, MD, Wataru Shimizu, MD, PhD, Kazuhiro Suyama, MD, PhD, Takashi Kurita, MD, PhD, Naohiko Aihara, MD, Shiro Kamakura, MD, PhD**

*From the Division of Cardiology, National Cardiovascular Center, Suita, Japan.*

**BACKGROUND** The electrophysiologic mechanisms of different ventriculoatrial (VA) block patterns during atrioventricular nodal reentrant tachycardia (AVNRT) are poorly understood.

**OBJECTIVES** The purpose of this study was to characterize AVNRTs with different VA block patterns and to assess the effects of slow pathway ablation.

**METHODS** Electrophysiologic data from six AVNRT patients with different VA block patterns were reviewed.

**RESULTS** All AVNRTs were induced after a sudden AH "jump-up" with the earliest retrograde atrial activation at the right superoparaseptum. Different VA block patterns comprised Wenckebach His-atrial (HA) block (n = 4), 2:1 HA block (n = 1), and variable HA conduction times during fixed AVNRT cycle length (CL) (n = 1). Wenckebach HA block during AVNRT was preceded by gradual HA interval prolongation with fixed His-His (HH) interval and unchanged atrial activation sequence. AVNRT with 2:1 HA block was induced after slow pathway ablation for slow-slow AVNRT with 1:1 HA conduction, and earliest atrial activation shifted from right inferoparaseptum to superoparaseptum without change in AVNRT CL. The presence of a lower common pathway was suggested by a longer HA interval during ventricular pacing at AVNRT CL than during AVNRT (n = 5) or Wenckebach HA block during ventricular pacing at AVNRT CL (n = 1). In four patients, HA interval during ventricular pacing at AVNRT CL was unusually long (188 ± 30 ms). Ablations at the right inferoparaseptum rendered AVNRT noninducible in 5 (83%) of 6 patients.

**CONCLUSION** Most AVNRTs with different VA block patterns were amenable to classic slow pathway ablation. The reentrant circuit could be contained within a functionally protected region around the AV node and posterior nodal extensions, and different VA block patterns resulted from variable conduction at tissues extrinsic to the reentrant circuit.

**KEYWORDS** Atrioventricular nodal reentrant tachycardia; Upper common pathway; Lower common pathway; Slow pathway ablation; Transitional cell zone; Ventriculoatrial block; Atrioventricular node; Posterior nodal extensions; Triangle of Koch

(Heart Rhythm 2006;3:544–554) 

## Introduction

Despite numerous studies on the electrophysiologic characteristics of atrioventricular nodal reentrant tachycardias (AVNRTs), controversy as to whether or not the reentrant circuit involves the atrium has been ongoing for several decades. Josephson et al[1–4] postulated that the reentrant circuit is contained within the AV node and that the circuit is connected to the atrium via AV nodal tissue called the "upper common pathway." In contrast, Jackman et al[5] hypothesized that the left side of the interatrial septum and the roof of the proximal coronary sinus form the upper link between the fast pathway and slow pathway (SP) and that a

**Address reprint requests and correspondence:** Dr. Kiyoshi Otomo, Department of Cardiovascular Medicine, Tsuchiura Kyodo Hospital, 11-7 Manabe-shin-Machi, Tsuchiura city, Ibaraki prefecture, 300-0053, Japan
E-mail address: k-otomo@fj8.so-net.ne.jp.
(Received November 14, 2005; accepted January 20, 2006.)

1547-5271/$ -see front matter  doi:10.1016/j.hrthm.2006.01.020